Abstract

JOHNSTON, JOE MONROE. Experimental Investigation of Bio-Inspired High Lift Effectors on a 2-D Airfoil. (Under the direction of Dr. Ashok Gopalarathnam).

Flaps mounted on the upper surface of an airfoil, called Lift Enhancing Effectors, have been shown to increase maximum lift and stall angle in wind tunnel tests. These effectors are fabricated from 0.35 mm thick Mylar and are allowed to rotate freely about their leading edges. The tests were done in the NCSU Subsonic Wind Tunnel at a chord Reynolds number of 4×10^5. The maximum lift coefficient was increased by up to 30% and α_{stall} was increased from 12° to at least 16°. Effectors were also fabricated out of stiff wood, allowing the deployment angle to be fixed with respect to the airfoil surface. This was not attempted in earlier research efforts and provided increased control in the current experimental study as the free-moving effectors tend to oscillate and their deployment angle cannot be controlled. Studying multiple fixed-deployment angles provided better understanding of the aerodynamics of the effectors and helped determine the optimal deployment angles. Fixed-deployment-angle effectors caused the zero-lift angle of attack to increase in proportion to the deployment angle. Drag tests on both the free-moving and fixed-deployment effectors showed marked improvement in drag at high alpha. The fixed-deployment-angle effectors showed drag improvement at increasingly higher alpha as deployment angle was increased. Oil flow visualization was conducted on the clean airfoil and the fixed-deployment-angle effectors. The surface flow pictured by these oil flow tests proved that the effector causes the separation point to move aft on the airfoil, as compared to the clean airfoil. This is thought to be the main mechanism by which the effectors improve both lift and drag. Finally CFD simulations were run and compared to the oil flow visualization. Results for separation point agree between oil flow and CFD, for most alphas. Lift tests indicate that increasing the deployment angle past 60° amounts to very little improvement in C_l. Drag tests show that the free-moving effector naturally produces a drag curve in between the curves for the 30° and 45° fixed effectors.

Experimental Investigation of Bio-Inspired High Lift Effectors on a 2-D Airfoil

by
Joe Monroe Johnston

A thesis submitted to the Graduate Faculty of
North Carolina State University
in partial fulfillment of the
requirements for the Degree of
Master of Science

Aerospace Engineering

Raleigh, North Carolina

2011

APPROVED BY:

Dr. Charles E. Hall Advisory Committee Member	Dr. Jack R. Edwards Jr. Advisory Committee Member

Dr. Ashok Gopalarathnam
Advisory Committee Chairman

Biography

Joe Johnston was born on November 27, 1985 in Salt Lake City, Utah to Jeffrey Johnston and Margaret Wheeler. He moved to Chapel Hill, North Carolina, at the age of 3, where he remained through high school. After graduating from East Chapel Hill High School in 2004, he matriculated at Middlebury College in Middlebury, Vermont. He graduated magna cum laude with a Bachelors of the Arts in Physics in May 2008.

After taking a year off to pursue work as an Emergency Medical Technician in Boston, Massachusetts, Joe started working towards his Master's degree at North Carolina State University in the fall of 2009. He joined the Applied Aerodynamics Group under the direction of Dr. Gopalarathnam after a semester at NCSU. His research has been largely experimental and has thus far resulted in a conference paper at the 29th annual AIAA Applied Aerodynamics Conference as well as this thesis.

Acknowledgements

First of all I would like to thank my advisor, Dr. Ashok Gopalarathnam. His guidance and support have been essential in both completing my thesis and making my graduate career successful.

I would also like to thank Dr. Hall and Dr. Edwards for being part of my committee. I have enjoyed working with both of them in classes and while doing research. Additionally I would like to thank Dr. Edwards for the CFD work he did in support of my research.

During my second year of graduate school at NCSU, I was financially supported by a fellowship from the Department of Defense SMART Scholarship. Additional support for my research was provided by the North Carolina Space Grant, a NASA program. These programs are gratefully acknowledged for their support.

My thanks goes to Stearns Heinzen for his help with the wind tunnel testing and Labview programming.

Finally I would like to thank my friends and family for their continued support throughout my schooling as well as the rest of my life.

Table of Contents

List of Tables

List of Figures

Nomenclature

C_l	2-D lift coefficient
$C_{l,max}$	Maximum 2-D lift coefficient
α	Angle of attack
α_{stall}	Angle of attack at which stall occurs
$C_l - \alpha$	Lift coefficient versus angle of attack curve
$^{x}/_{c}$	chordwise position as a fraction of chord length
Re	Reynolds number
θ	Deployment angle of the effector; angle between the airfoil upper surface and the effector lower surface
C_p	Coefficient of pressure
C_d	2-D drag coefficient
$C_d - \alpha$	Drag coefficient versus angle of attack curve
C_m	2-D pitching moment coefficient, taken about the quarter chord
$C_m - \alpha$	Pitching moment coefficient versus angle of attack curve

Chapter 1

Introduction

In engineering it is often the goal of the engineer to improve upon a design in order to change or enhance the desired design characteristics. However, there are times when the usual modes of improvement become stale and no longer produce significant changes. At times like these engineers have looked to nature in order to find new methods [1, 2]. The designs found in this manner can be called bio-inspired designs. Many examples of this bio-inspired engineering exist in the world around us: Velcro for instance was inspired by the impressive grasping ability of the common burr.

Aeronautical engineers have also used bio-inspired engineering in the past. Da Vinci's ornithopter, while unsuccessful, is a prime example. Several more examples, particularly in respect to fluid dynamics, can be found in articles by Bechert et al. [1, 2]. Of interest here is the application of a device to control flow separation on a wing. Separation is directly linked to loss of lift, or stall, and is therefore of vital importance to the study of fixed-wing flight. Controlling separation is an effective way of increasing both the maximum lift produced by a wing and the stall angle of attack. It has been seen that birds have an efficient means of doing this with feathers on the upper surface of the wing [3]. These feathers, called upper-wing coverts, rise off the surface of the wing when they encounter separated flow and this seems to aid in allowing the bird's wings to continue producing lift at high angles of attack, such as during perching maneuvers [3]. The goal is now to reproduce a similar effect on man-made wings for application to aircraft.

Recent studies on what we will call Lift Enhancing Effectors, or just effectors, have proven their ability to increase both $C_{l,max}$ and α_{stall} at a range of Reynolds numbers. The effectors themselves are flaps, attached at their leading edges to the upper surface of the wing and allowed to rotate freely (Figure 1.1).

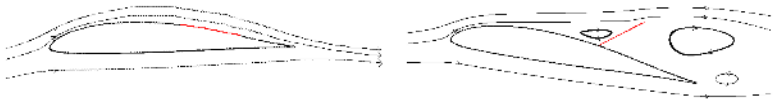

Figure 1.1: A drawing showing an airfoil with an effector attached (shown in red) at two angles of attack. At low α the effector should lie flat against the airfoil surface whereas at high α the effector deploys and delays separation on the airfoil.

Bechert et al. discuss the method by which these effectors function [1, 2]. Reversed flow, which occurs in the separated flow regime, lifts the effector by its trailing edge. Once lifted, or deployed, the effector acts as a pressure dam, effectively blocking the separation from progressing further towards the wing's leading edge and therefore allowing more of the wing to continue experiencing attached flow and producing lift. Bechert et al. [1, 2] proved the viability of the Lift Enhancing Effector in the Reynolds range of $1 \times 10^6 - 2 \times 10^6$. Kernstine et al. [4] extended the study to the lower Reynolds range of $1 \times 10^5 - 5 \times 10^5$ and Schlüter [5] proved the effectiveness at the very low Reynolds range of $3 \times 10^4 - 4 \times 10^4$.

The effectors are proven at a wide range of Reynolds numbers, but it is still important to know how to fabricate and configure them. Several studies have noted detrimental effects in the low drag region when effectors are attached to the airfoil. Lift production is decreased whereas drag is increased. This has been attributed to early deployment of the effectors causing separation or early transition to turbulent flow [1, 2]. Bechert et al. state that the area under the effector is connected to a higher pressure zone than the area just above. This causes the effector to slightly deploy even at low angles [1, 2]. Several methods have been suggested to combat this early deployment, including locking the effectors down until they are needed at high α. However, the most popular method is to use either a porous material or a jagged trailing edge on the effector to allow the pressures on either side to equalize and therefore keep the effector smooth against the surface of the airfoil [1, 2, 6, 7].

Another factor influencing effector fabrication is material selection. To avoid the detrimental effects discussed in the preceding paragraph, the effector needs to follow the contour of the airfoil. Therefore the effector should be made of a material which is both flexible and thin [4]. This allows the effector to lie flat against the airfoil surface at low-α, and still function properly at high-α. A flat, rigid effector will be unable to follow the airfoil surface and will cause separation at its trailing edge. If the effector is too thick it will act like a ridge at its leading edge, causing early transition, an obvious disadvantage especially for natural laminar flow airfoils. However, Kernstine et al. noted that the material must remain strong or it will tend to tear as a result of aerodynamic forces [4].

Having discussed the material used in fabricating the effectors, we now move on to the size and chordwise placement on the airfoil. Meyer et al. found that increasing the size of the effector increased the resulting gains in lift [6]. However, there seems to be a limit to size of the effector due to weight considerations. In order to respond to the relatively low velocities of reversed flow, the effector must be kept light. Most studies have chosen an effector length between 10 and 30 percent of the airfoil chord. Kernstine et al. focused on the chordwise placement of the effector and found [4] the greatest increases in lift to occur when the effector was placed with its leading edge closer to the front of the airfoil, around 0.2 x/c. Other studies have mentioned the undesired effect of early transition as a reason to keep the effectors farther aft on the airfoil [6] and indeed Kernstine et al. saw greater drag along with the lift increase when the effector was moved forward [4]. To keep drag at a minimum while also gaining from the lift enhancing properties of the effector it seems best to place the effector aft of the 0.5 x/c location on the airfoil. However, as noted by Bechert et al., the trailing edge of the effector must remain at least 0.1 x/c forward of the airfoil trailing edge in order to properly respond to flow separation [1, 2].

The above discussion shows that these effectors have been proven as a viable method of increasing lift and α_{stall}, but they still constitute a relatively novel approach and therefore merit further research. In particular the optimal deployment angle of the effector has not been studied in detail. This research attempts to do just that. Using the NCSU subsonic wind tunnel and an airfoil model with surface pressure taps, we look at the changes in the aerodynamic characteristics due to an effector at several different angles of deployment, as measured from the surface of the airfoil. Along with studying a free-moving effector, deployment angle is studied in detail using a rigid effector set at several different fixed-deployment angles, where the effector remains stationary with respect to the airfoil throughout the α range. For both types of effectors, coefficients of lift and drag were determined using pressure scans. Lift was calculated from surface pressure distributions and drag from pressures in the wake of the airfoil, using a momentum loss method [8]. Surface flow visualization was also employed to find separation points and better understand the effects on the flow over the airfoil. Finally the fixed-deployment-angle effector was modeled in a computational fluid dynamics code, which gives us further understanding of the manner in which flow reacts to the presence of the effector.

Chapter 2

Experimental Set-Up

2.1 Wind tunnel and Airfoil Model

Experiments were carried out in the NCSU subsonic wind tunnel. This is a closed-circuit, low speed tunnel. The test section is 0.81 m high, 1.14 m wide, and 1.17 m long and has a maximum wind speed of approximately 40 $^{m}/_{s}$, allowing for a maximum chord Reynolds number of approximately 6×10^5 for an airfoil model with a 1ft. chord. The tunnel turbulence factor has been calculated using a pressure sphere test [8] and was found to be approximately 1.5.

The airfoil model used is mounted vertically and has nine identical spanwise sections which, when all nine are used, span the test section, creating approximately 2-D flow. The model has a chord of 30.5 cm with a 20% chord trailing edge flap, which was kept at 0° deflection for the current work. Pressure taps are located around the surface of each model section with 40 taps around the main body and 10 around the trailing edge flap. During the testing only the taps on the center section were used and, because of a limiting number of inputs to the digital pressure system, only 4 taps on the flap were used, 2 on the upper surface and 2 on the lower surface. This model was chosen due to the presence of the pressure taps and because of its availability. It was originally built for use in the NCSU subsonic tunnel and is described in detail by Jepson and Gopalarathnam [9].

2.2 Pressure System

Pressure measurements were taken with a digital scanning system. Three Scanivalve DSA 3217 units with 16 input channels provide a total of 48 channels. For lift tests 44 of the channels were used — each corresponding to one of the pressure taps on the airfoil model. These 44 measurements allow for a detailed view of the pressure distribution over the full airfoil surface. Lift coefficients were calculated from the pressure distribution. For the drag tests 36 channels were used — 16 for the wake rake and 20 for surface pressures. This allows for drag to be computed from the wake pressures and angle of attack to be verified with the surface pressures. The wake rake was a traversing rake which collected pressure data every $1/16$ in.

2.3 Effector Fabrication

In order to test the Lift Enhancing Effector it was necessary to fabricate several effectors to fit the airfoil model. Based on the observations of previous researchers, 0.35 mm Mylar was chosen as the material for the free-moving effector. This provides a lightweight, flexible effector which responds well to low-velocity reversed flow. The Mylar effectors were attached to the model with tape at the effector's leading edge (Figure 2.1a).

For the effectors set at fixed-deployment angles, a more rigid material was required to maintain the effector position during testing. Oak wood sheet of 6.35 mm thickness was chosen for its relative stiffness as well as the ease with which it could be cut to appropriate size. A separate effector was built for each angle tested. The effector's leading edges were cut at an angle to meet smoothly with the airfoil surface and triangular brackets were attached to the underside of each effector to hold the desired deployment angle (Figure 2.1b). Velcro strips were attached to the airfoil surface and the triangular brackets to act as the attachment between the effector and the airfoil. Each fixed-angle effector also had a strip of tape attached between its leading edge and the airfoil in order to cover the small space left there.

(a) (b)

Figure 2.1: Inset a: The airfoil model in the NCSU subsonic wind tunnel with the effector attached. Inset b: The airfoil with a fixed-deployment-angle effector attached.

2.4 Flow Visualization

Flow visualization was done in order to determine the separation point as well as obtain an understanding of the air flow over the surface of the model. The technique used was oil flow visualization, as described in Chapter 5 of *Low Speed Wind Tunnel Testing* [8]. An oil mixture is applied to the surface of the model before starting the wind tunnel. After the tunnel is stopped the patterns in the oil show how the air flows across the surface of the model. First the model was covered with a black coating, both to protect the pressure taps from clogging and to provide a good background on which to see the white oil. Then a mixture of SAE 20 and SAE 40 oil, with powdered titanium dioxide added to whiten the mixture, was painted across the center section of the model. For each angle of attack studied, the model was first set at the appropriate angle and then coated with oil. The wind tunnel was started and brought up to speed and allowed to run for several minutes. Once the oil settled into a stable pattern the tunnel was stopped and pictures were immediately taken so the flow could later be studied in detail.

Chapter 3

Experimental Results

3.1 Lift Tests

3.1.1 Validation

Jeff Jepson [9] conducted tests to validate the wind tunnel results for the airfoil model used. Since this study uses the same wind tunnel and the same model, these validation results can be extended to the current work. Early tests of the airfoil model in the current work also showed that the $C_l - \alpha$ curves from wind tunnel experiments match well with the predicted curve from XFOIL at the same Reynolds number, as shown in Figure 3.1. The curves are seen to match quite well, especially considering that XFOIL typically over-predicts α_{stall} and C_l at high angles of attack, in comparison to wind-tunnel experiments.

3.1.2 Free-Moving Effector

The first tests of the free-moving effector were done in order to determine the best test conditions and effector configuration. Based on the observations by Kernstine et al. [4] and Bechert et al. [1, 2] it was determined that the effector leading edge should be aft of the 0.5 $^{x}/_{c}$ location, but with the trailing edge forward of the airfoil trailing edge. Four initial configurations were tested and compared with the clean airfoil. An effector of length 10% of the airfoil chord was tested with the leading edge at 0.8 $^{x}/_{c}$ and at 0.7 $^{x}/_{c}$. An effector of length 20% of the airfoil chord was tested with the leading edge at 0.8 $^{x}/_{c}$ and 0.6 $^{x}/_{c}$. All four configurations were tested at a chord Reynolds number of 4×10^5. The resulting $C_l - \alpha$ curves are shown in Figure 3.2. Pressure data was taken at each alpha for both increasing-α and

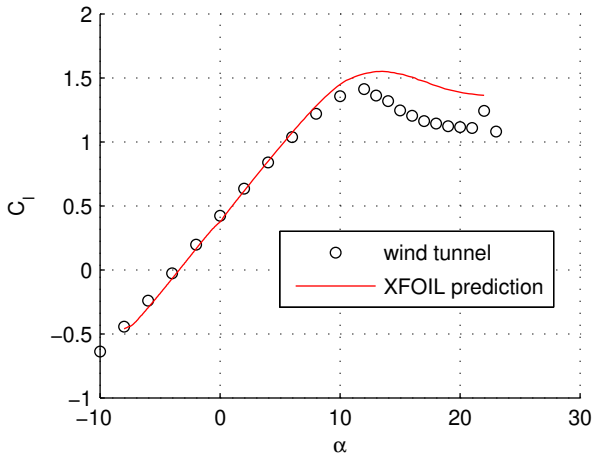

Figure 3.1: C_l curves for the clean airfoil from XFOIL and from wind tunnel tests.

decreasing-α sweeps for each configuration. No hysteresis was present in the results, with the exception of when the effector flipped over entirely and was unable to return to its normal position during the decreasing-α sweeps. However, care was taken to avoid this problem and returning the effector to its normal position by hand proved to avoid the hysteresis. Unless otherwise noted, only data from the increasing-α sweeps will be reported from here on.

As can be seen in Figure 3.2, no significant gain in C_l was seen at the airfoil's normal stall angle. However, C_l was maintained to a much higher angle of attack and the stall characteristic was seen to become very gentle in comparison to the clean airfoil. Although it was hoped that the Lift Enhancing Effector would lead to an increased $C_{l,max}$, these results are nonetheless positive. Another departure from previous work was the tendency of the effectors to oscillate once deployed. This was also seen by Traub and Jaybush [7] but is absent from the other studies. The reason for some effectors to oscillate whereas others remain stable is yet to be determined, but there is no cause to believe that the oscillation has any detrimental effects.

These initial tests were all carried out with partial span effectors, extending over the middle third of the airfoil model. This set-up could introduce some 3-D effects into the flow, but those effects should have been confined to the areas near the edges of the effectors. Since pressure data was taken only from the center section, any 3-D effects should have been minimal and the results are still valid as a tool for checking the use of the effectors. Based on those initial tests, the 20% chord effector located with its leading edge at 0.6 x/c was chosen as the configuration to use for all further testing. This choice was

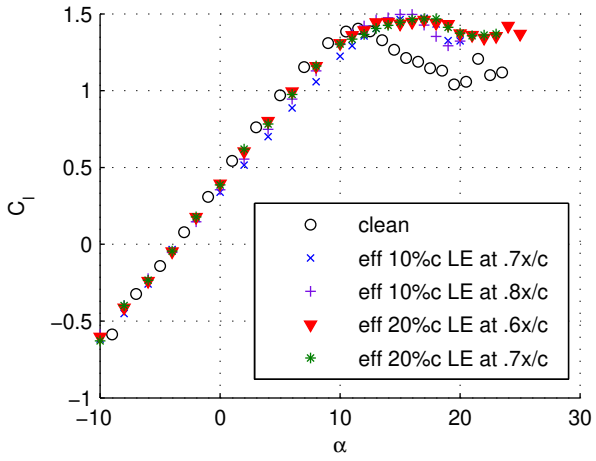

Figure 3.2: C_l curves from the initial tests of various effector configurations

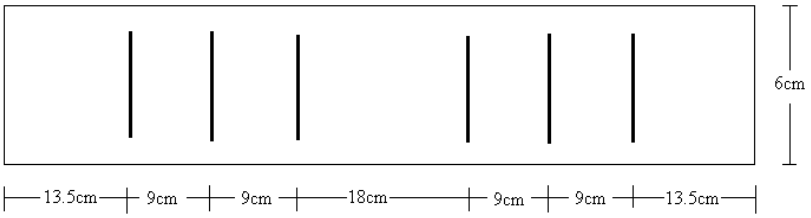

Figure 3.3: A sketch of the Mylar effector showing the locations of the pressure-equalizing slits.

made due to the minimal loss of lift seen at low alpha (particularly the 0 to 10 degree range), as well as the continued production of lift at alpha higher than seen for other configurations (Figure 3.2).

Tests were next done using a full span version of the configuration chosen above. These tests showed the early deployment problem encountered in several preceding studies [1, 2, 6, 7]. In previous work a jagged trailing edge has been used to combat this problem [1, 2, 7], but for this study it was decided to attempt to equalize the pressure on either side of the effector by cutting several chordwise slits in the material. Although this technique did not cause any obvious visible change in the early deployment it show some improvement in terms of increasing C_l at low alpha and a stabilizing effect was observed on the effector's flutter. With the slits, the effector still oscillated between deployment angles, but the amplitude of the oscillation was seen to decrease. For these reasons the slits were kept as a part of the effector. Six slits were made in the effector, as is shown in Figure 3.3.

A test at an increased Reynolds number of 5×10^5 caused tearing to occur in the effector. Therefore the rest of the tests were conducted at the original 4×10^5. The $C_l - \alpha$ curve resulting from experiments

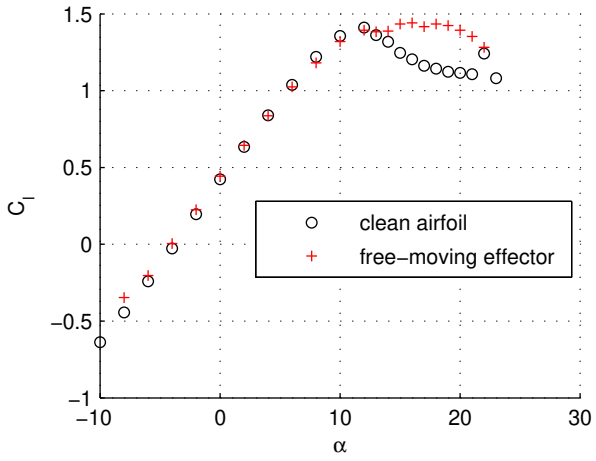

Figure 3.4: The C_l curve from the full length effector in its final configuration compared to the curve from the clean airfoil.

carried out with the final configuration at Re 4×10^5 can be seen in Figure 3.4. $C_{l,max}$ increases from 1.41 at $\alpha = 12°$ for the clean airfoil to 1.44 at $\alpha = 16°$ for the effector equipped airfoil. At $\alpha = 16°$ this represents a 0.24 increase in C_l, an almost 17% gain in C_l and a 4° increase in the stall angle. The greatest C_l increase was 0.30 at $\alpha = 19°$, a gain of almost 27%. Despite the lack of a large increase in C_l at the airfoil's original stall angle, the effector clearly has favorable effects on the lift producing capability of the airfoil, particularly at high angles of attack. This is roughly what was expected from literature and is what the effector is meant to accomplish. Stall is extended from $\alpha = 12°$ for the clean airfoil to approximately $\alpha = 20°$ for the effector equipped airfoil. There is a slight dip noticeable in the curve for the effector equipped airfoil at $\alpha = 12°$ which is not understood at this time. This dip did not occur in earlier tests with the same configuration.

Since the lift coefficients were found using a pressure distribution method, we also have available the C_p distributions for each alpha tested. Examining some of these gives us some insight into how the effector works. Figure 3.5 shows the comparison of C_p distributions between the effector equipped airfoil and the clean airfoil at $\alpha = 4°$. Just before the leading edge of the effector a distinct drop in the pressure is evident. This is evidence of a stagnation point caused by the slight ridge where the effector is attached to the airfoil. Since the effector material and tape used to attach the effector to the airfoil were both very thin, it appears that this stagnation could only be avoided by nesting the effector in the surface of the airfoil. This was impossible for our tests because altering the airfoil would have disrupted the pressure taps and made data acquisition impossible.

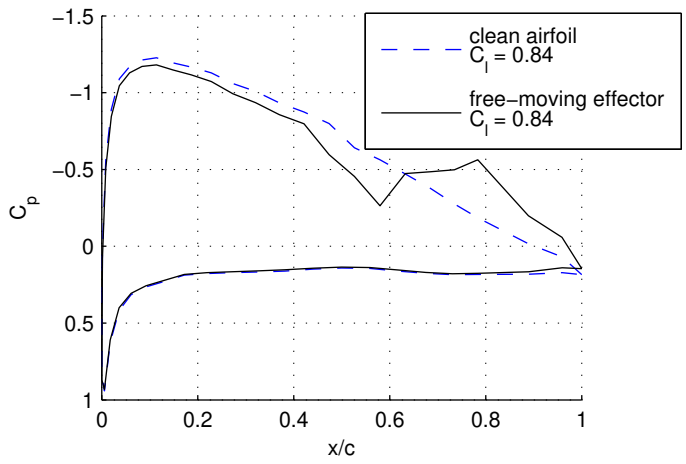

Figure 3.5: C_p distributions at $\alpha = 4^o$ for the clean airfoil and the airfoil with the free-moving effector.

The pressures shown between $x/c = 0.6$ and 0.8 are directly under the effector. These pressures appear to be lower than the pressure both fore and aft of the effector. Bechert et al. claim that the area under the effector is connected to a slightly higher pressure causing premature deployment [1, 2]. The lower pressure seen in Figure 3.5 seems to be due to the pressure equalization accomplished by cutting slits in the effector. The higher pressure mentioned by Bechert et al. was seen for the C_p distribution when no slits were cut in the effector. Although a small amount of premature deployment was observed during this test, a much greater decrease in C_l was seen in later tests with an effector without slits.

Finally it can be seen that the C_l reported is only slightly lower for the effector equipped airfoil. However, it must be noted that because the effector is not deployed, the pressure taps directly underneath it are not connected to the lift producing flow. Removing the data from these taps and averaging pressure from the taps just in front of and just behind the effector gives us a slightly decreased C_l of 0.80 for the free-moving effector at $\alpha = 4^o$. It can be seen that this decrease in the lift is due mainly to a decreased suction peak. It seems likely that the stagnation point just in front of the effector causes an increase in C_p which propagates forward all the way to the leading edge and therefore decreases the overall C_l. Another small effect on C_l comes from the slightly decreased pressure at the airfoil's trailing edge which decreases the lower surface pressure on the aft section of the airfoil. As will be noted in the following section, this trailing edge behavior is the opposite of the behavior when the effector is deployed at high α.

Once the effector is deployed, the issue of some pressure taps being covered disappears and data from all of the taps can be considered valid both for examining the pressure distribution and calculating C_l.

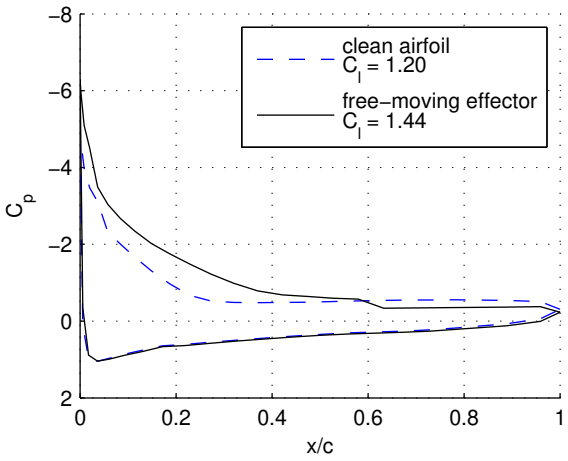

Figure 3.6: C_p distribution at $\alpha = 16^o$ for the clean airfoil and the airfoil with the free-moving effector.

Figure 3.6 shows the C_p distribution for the effector equipped airfoil compared to the clean configuration at $\alpha = 16°$. This is the angle of attack for which the effector equipped airfoil had its $C_{l,max}$ and the reason for the improvement over the clean airfoil is evident in the C_p distribution. The pressure on the upper surface in front of the effector is lower than for the clean airfoil, allowing more lift to be produced. This is accomplished by allowing the pressure to decrease in a stepwise manner across the effector as described by Bramesfeld and Maughmer [10]. Behind the effector the pressures are increased compared to the clean version. Although the stepwise pressure change means that less lift is produced by the part of the airfoil aft of the effector, this is partially offset by the effector allowing a higher trailing edge pressure and therefore higher pressures on the airfoil's lower surface.

3.1.3 Fixed-Deployment-Angle Effectors

In order to better understand the importance and effect of the deployment angle, tests were carried out with a rigid wood effector set at several fixed-deployment angles. From here on the deployment angle of the effector, with respect to the airfoil surface, will be denoted by the symbol θ. Previous studies concluded that allowing the effector to deploy past 90° with respect to the airfoil surface could not produce any further benefits [1, 2]. This makes sense because for the effector to freely deploy past 90°, the top of the separated layer must be higher than the top of the effector and the effector would therefore no longer be able to influence the flow. Accordingly, the largest fixed-deployment angle was chosen as 90°. Five other angles were chosen to give a representation of the full range. These angles

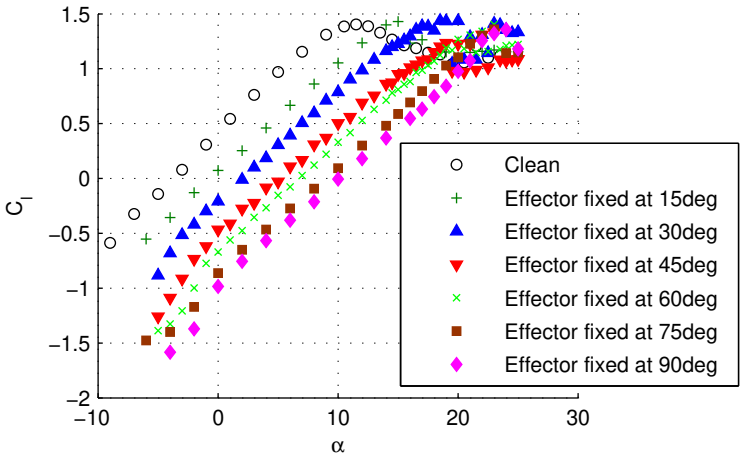

Figure 3.7: C_l curves for the clean airfoil and the 6 fixed-deployment effectors.

were $\theta = 15°$, $\theta = 30°$, $\theta = 45°$, $\theta = 60°$, and $\theta = 75°$. As with the free-moving effectors, each fixed effector was 20% of the airfoil chord in length and fixed to the airfoil with the effector leading edge at 0.6 x/c. The Reynolds number for each test was 4×10^5.

The resulting $C_l - \alpha$ curves are shown in Figure 3.7. The first characteristic one notices in these plots is the reduction in C_l for a given pre-stall α as deployment angle is increased: in other words, the zero lift angle of attack increases with the deployment angle. This would suggest that the effector causes an effective reduction in camber in proportion to the amount by which the effector is deployed. This result is also consistent with CFD results from Meyer et al. [6]. When the effective camber is decreased the airfoil produces the same amount of lift as it would at a much lower geometric angle of attack. This serves to give some insight into the manner in which these effectors function and it also quite clearly shows that any effector used in application on a real wing would have to be able to operate through a continuous range of deployment angles. Actuating such a device to finite angles might cause a sudden drop in lift, which could be detrimental to the performance of an aircraft in flight.

Another trend, which can be noted in Figure 3.7, is the apparent lack of continued increase in $C_{l,max}$ as deployment angle is increased. The largest value of C_l occurs with the effector set at $\theta = 30°$. However, the larger deployment angles reach their own $C_{l,max}$ at higher α than that for the 30° effector. This can be interpreted in several ways. First, perhaps there is no need to allow the effector to deploy past 30°. However, the large fluctuations in C_l after $\alpha = 20°$ for all configurations except $\theta = 90°$ make it difficult to interpret the results at these very high angles of attack. It is possible that the effector needs to be

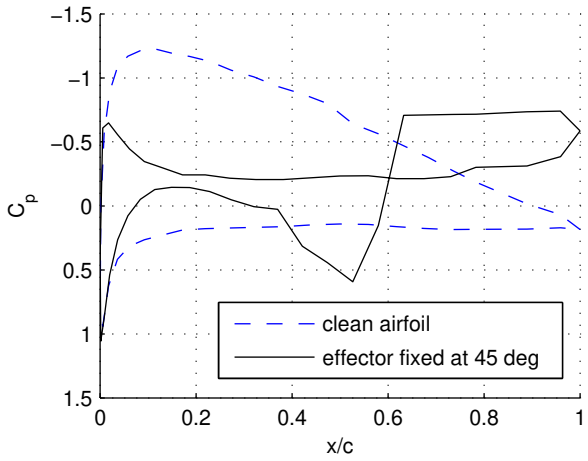

Figure 3.8: C_p distribution at $\alpha = 4^o$ for the clean airfoil compared to the effector fixed at 45° deployment.

deployed past 30° in order to continue producing the lift coefficients seen with the free-moving effector at very high α.

The largest gain in C_l occurs at $\alpha = 23°$ with the effector deployed to 60°. At this angle there is an approximately 30% increase in lift over the clean airfoil. In comparison, with the effector fixed at $\theta = 30°$, the $C_{l,max}$ is 1.44 at $\alpha = 18.5°$. This is a gain of approximately 27% over the clean airfoil. This configuration is also the only one to have a $C_{l,max}$ greater than that of the clean airfoil and it occurs closest of the six to the angle of attack for which the $C_{l,max}$ occurs with the free-moving effector. The angle at which $C_{l,max}$ occurs progress from 15° at $\theta = 15°$ to 18.5° at $\theta = 30°$ and then 23° for $\theta = 45°$. For $\theta = 60°$ and 75° the angle for $C_{l,max}$ remains 23° and then increases again to 24° for $\theta = 90°$. This would suggest that 45° is the greatest value of θ needed to achieve the maximum increase in α_{stall}. However the $C_{l,max}$ at $\theta = 45°$ is only 1.33 whereas at $\theta = 60°$ it reaches 1.40. Based on these results it seems that $\theta = 60°$ may be the optimal maximum deployment angle, especially since $C_{l,max}$ is lower than 1.40 for both $\theta = 75°$ and $\theta = 90°$.

At low-α, the C_p distribution for the airfoil with the effector fixed is very different from the clean airfoil. This is shown in Figure 3.8 for the airfoil at $\alpha = 4°$ with the effector fixed at $\theta = 45°$. The lift is effectively destroyed by having the effector deployed at this low angle of attack. The effector seems to be acting like a spoiler at this point and in fact negative lift is being produced forward of the effector. The C_p distributions are similar for all of the fixed-deployment angles at low-α.

Table 3.1: Activation angles for the fixed-deployment-angle effectors.

ϑ	Activation Angle
15 °	14 °
30 °	16 °
45 °	18 °
60 °	19 °
75 °	20 °
90 °	21 °

As α increases, the C_p distributions from the airfoils with fixed effectors attached become more and more like the distributions seen for the free-moving effector. If we take the presence of a pressure step, as described by Bramesfeld and Maughmer [10] and seen in Figures 3.6 and 3.9, to signify that the effector is functioning properly to increase lift, the C_p distributions for the fixed effector tests can be used to find the α at which the effector at each deployment angle becomes active. These angles are given in Table 3.1. These 'activation angles' are remarkably close to the angle of attack at which the $C_l - \alpha$ curve for each fixed-deployment-angle effector crosses the $C_l - \alpha$ curve of the clean airfoil. The distribution at $\alpha = 18°$ is shown for the clean airfoil as compared to the airfoil with the effector fixed at $\theta = 30°$ in Figure 3.9. It is notable that the C_p distributions for the fixed effector and the free-moving effector, at this angle of attack, are very similar (Figure 3.6). The other fixed effectors are not shown, however, the C_p distributions for each of the configurations, once active, follow the same trend and show a distinct pressure step. It is seen that as the fixed-deployment angle is increased, the α at which the effector becomes active increases. This observation suggests that as α increases, the effector needs to deploy to a higher θ in order to continue the improvement in the lift of the airfoil. This is also shown in the numerical results from Meyer et al. [6] and can be understood at a basic level by recognizing that the effector's trailing edge will just touch the edge of the separated boundary layer when it is active. As α increases, the separation layer becomes thicker and so the effector will have to deploy to a higher angle in order to maintain contact.

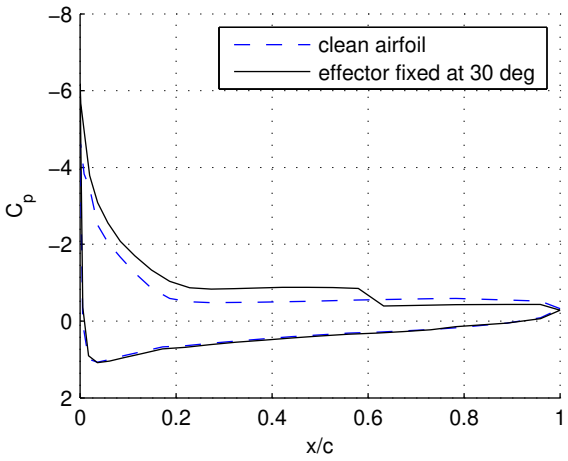

Figure 3.9: C_p distribution at $\alpha = 18^o$ for the clean airfoil compared to the effector fixed at 30° deployment angle.

3.2 Drag Tests

Profile drag can be measured on this model using a momentum loss method as described in Barlow et al. [8]. Pressures across the wake behind the model were measured and the drag was computed from the difference in momentum in front of the model, where pressure is equal to the free-stream pressure, and behind the model, where pressures are influenced by the wake. However, this method requires the use a wake rake which needs 16 pressure lines. Since the model uses 44 pressure lines for surface pressure and only 48 channels are available on the DSA units, it was impossible to get a full scan of the surface pressure for C_l calculation and find drag during the same test, so the lift and drag tests were performed separately. During the drag tests, 20 of the surface pressure taps were connected to take data along with the wake rake. While this does not give enough surface data to compute lift, it does allow the airfoil C_p distribution to be compared between the drag tests and the lift tests. Comparing these distributions serves as a way to verify the angle of attack during the drag tests. As with the lift tests, all drag experiments were carried out at a chord Reynolds number of 4×10^5.

3.2.1 Repeatability

Drag tests were completed for all of the effector configurations, including free-moving and all six of the fixed-deployment angles, as well as the clean airfoil. Before beginning these drag tests some repeatability tests were done to ensure that lift and drag measurements taken at separate times could be

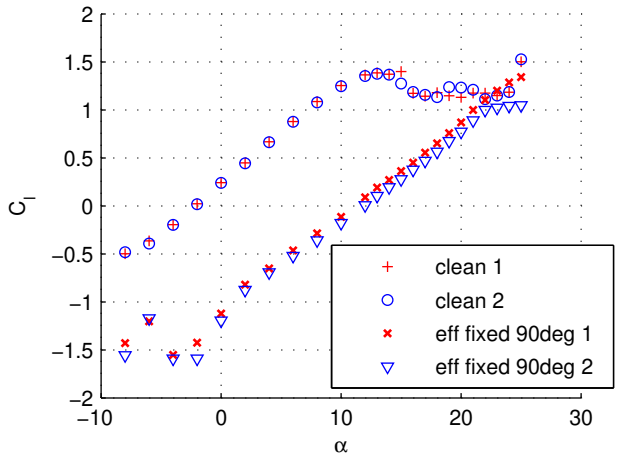

Figure 3.10: Repeatability tests. Lift data taken for the clean airfoil and the airfoil with the effector fixed at 90 degree deployment. Runs 1 and 2 were done several days apart.

considered together. Repeatability was confirmed by performing the same tests several days apart. Both the clean airfoil and the airfoil with the fixed-deployment effector at 90° were checked for repeatability. It was assumed that the repeatability results from the one fixed-deployment angle could be extended to all the fixed angles. Figure 3.10 shows the lift curves found during these tests. The two curves for the clean airfoil are almost identical, at least up to stall, proving the repeatability of the test. However, there is a small offset in the curve for the fixed effector. This offset is believed to be caused by the mounting of the effector. Due to the method of attaching the effector to the airfoil, small changes in the exact position of the effector are possible each time it is removed and reattached to the airfoil. Drag testing was completed regardless, but it is important to note that this offset creates a small amount of uncertainty in the data.

Another difference in the tests for lift and drag comes from the model's position in the wind tunnel test section. For lift tests the model is mounted at the center of the test section. For drag tests, however, the model must be mounted farther forward in the test section. This allows for room to mount the wake rake behind the model. Even with the model moved all the way to the front of the test section, the wake rake is mounted just less than two chord lengths downstream of the model. As shown in Figure 3.11 there is some small change in the lift curves for the airfoil in the two different mounting positions. With the fixed effector attached, however, the change could be due to either the position of the model or the mounting of the effector, as discussed in the preceding paragraph. The slight changes in the lift curve for the clean airfoil however can be more directly attributed to the position of the model in the tunnel

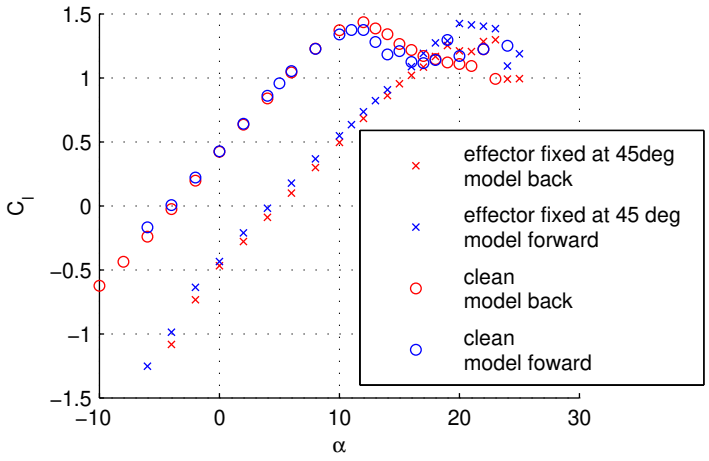

Figure 3.11: Comparison of lift curves with the model mounted in the center of the test section (model back) and at the front of the test section (model forward).

test section. As with the repeatability tests, these changes were not deemed so great as to make the drag tests invalid, but again it must be noted that there is a small change which affects the results of the drag tests.

3.2.2 Drag

Kernstine et al. [4] reported a decrease in drag at high alpha with an effector mounted on the aft section of the airfoil's upper surface. Figure 3.12 shows similar results in this study. At angles of attack below normal stall for the airfoil, drag is virtually unaffected. This is the desired result. As with lift, the effector should not change the performance of the airfoil in the pre-stall regime. Once the airfoil stalls, however, the effector equipped airfoil experiences less drag. This is the same region in which the effector equipped airfoil experiences an increase in lift and again is the desired result. Another feature to note in Figure 3.12 is the hysteresis apparent for the airfoil with the effector; an increase in drag is clearly shown for the decreasing-α sweep. The improvement in drag over the clean airfoil is maintained despite this increase; however, the reason for the hysteresis is currently unknown. The decreasing-α sweep was only run from $\alpha = 23^o$ to $\alpha = 12^o$.

Drag on the clean airfoil starts to increase at $\alpha = 10°$ and dramatically increases after stall at $\alpha = 12°$. With the free-moving effector equipped, the low drag region for the airfoil is extended to $\alpha = 14°$. Although stall for the effector equipped airfoil does not happen until approximately $\alpha = 20°$,

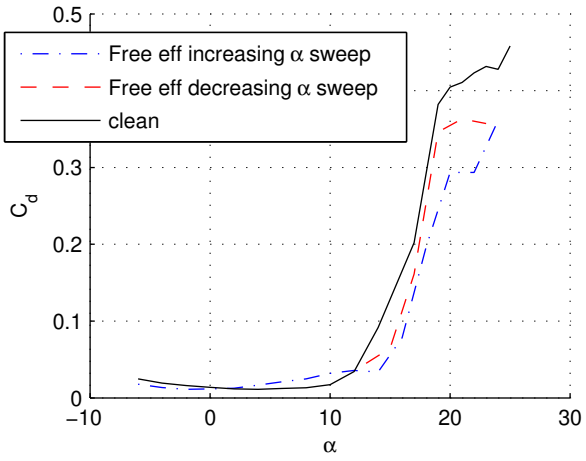

Figure 3.12: Drag coefficient versus alpha for the airfoil with the free moving effector as compared to the clean airfoil. A shortened downwards sweep with the effector equipped airfoil shows some hysteresis.

the increase in drag occurs well before that point. From $\alpha = 14°$ to $\alpha = 20°$ the airfoil with the free-moving effector experiences a decrease in drag coefficient of 0.075 to 0.1 (for the increasing-α data). At $\alpha = 14°$ this is 75% less drag than the clean airfoil.

For the fixed-deployment-angle effectors drag tests showed similar trends as the lift tests. Each successively higher deployment angle creates more drag in the low alpha range, similar to how it decreases lift in the low alpha range, but maintains its own low drag region to a higher alpha than the previous deployment angle. This is shown in Figure 3.13. Drag for the $\theta = 90°$ effector is not shown because as of this writing the test has not been completed at the appropriate Reynolds number. In the low alpha range the fixed-deployment effector acts like a spoiler. It extends through the boundary layer and into the freestream. This forces separation on the airfoil and also creates a much larger wake than the airfoil would normally have. So at low alpha the fixed effector clearly has a detrimental effect, greatly increasing drag and at the same time decreasing lift. However we begin to see some improvement as alpha is increased beyond the normal stall point. The dramatic increase in drag, which generally accompanies stall and starts at $\alpha = 10°$ for the clean airfoil, does not start until $\alpha = 12°$ for the $\theta = 15°$ case and starts successively later for the larger deployment angles. This is quantified in Table 3.2. The angle at which each fixed-deployment effector first shows improvement in lift over the clean airfoil is of course much earlier, between $\alpha = 10°$ and $\alpha = 15°$ for all values of θ. Comparing this to Figure 3.7 one may note that the improvement in drag occurs at a lower alpha than does the improvement in lift.

Table 3.2: Angle of attack at which drag begins to increase for the clean and fixed-deployment effector cases.

θ	Beginning of Drag increase (α)
clean	10°
15°	12°
30°	15°
45°	18°
60°	20°
75°	22°

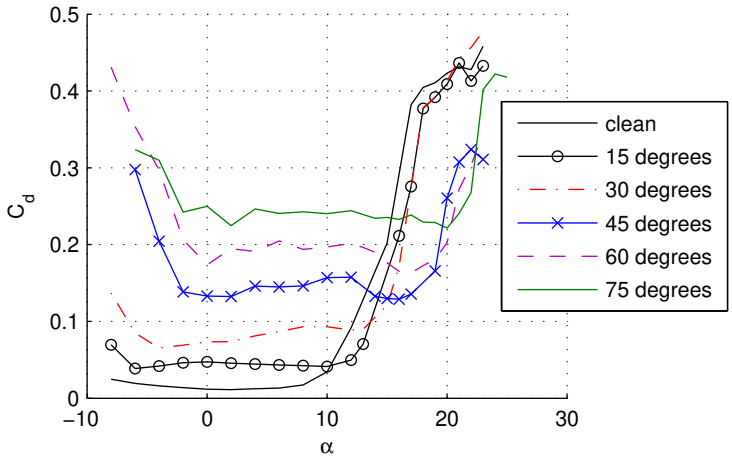

Figure 3.13: Drag coefficient versus alpha for the airfoil with the fixed-deployment-angle effectors.

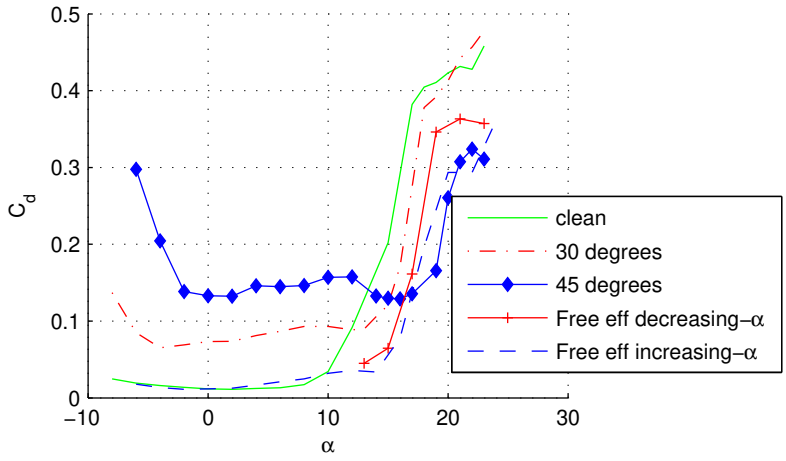

Figure 3.14: Drag coefficient versus alpha for the free moving effector compared to the fixed-deployment-angle effectors.

When comparing the free moving effector to the fixed-deployment effectors (Figure 3.14), the curve for the free moving effector lies between the curves for the fixed-deployment effector at $\theta = 30°$ and $\theta = 45°$ in the high drag regime. This could suggest that the average deployment angle, when the effector is allowed to move freely, is somewhere around 35 or 40 degrees. This also goes along with the conclusions drawn from lift tests.

3.3 Pitching Moment

Using the same pressure data that was used to determine lift coefficients, the coefficient of pitching moment was also calculated for each of the configurations. The pitching moment was taken about the quarter chord, as is the convention.

3.3.1 Comparison with XFOIL

Figure 3.15 shows the $C_m - \alpha$ curves for the clean airfoil. The red data are taken from XFOIL analysis of the airfoil in the viscous mode at a chord Reynolds number of 4×10^5. This is compared with the experimental data, which is also taken at $Re = 4 \times 10^5$. The XFOIL predictions are slightly more positive at all angles of attack. However, the gap is relatively small and the data follow the same trends. The pitching moment is negative at all alpha except $\alpha = -10°$ and stays fairly constant from $\alpha = -6°$ to α_{stall}, $\alpha = 12°$. Just before stall, C_m becomes slightly more positive and after stall the

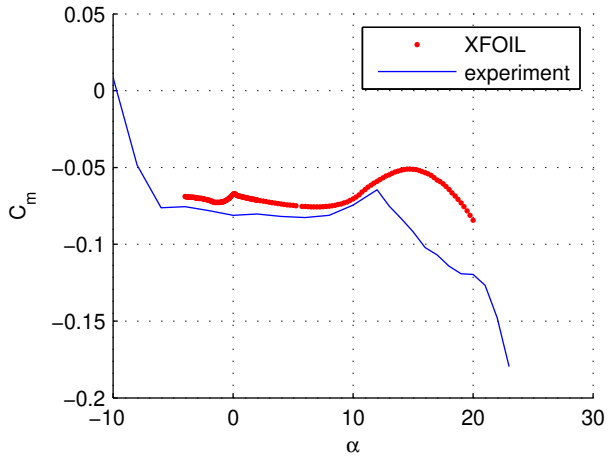

Figure 3.15: $C_m - \alpha$ curve for the clean airfoil at Re 4×10^5 from experiment and from XFOIL analysis.

curve slopes downwards, becoming more and more negative. XFOIL predicts the rise and fall of C_m at slightly higher alpha which could be connected to the higher prediction for α_{stall} as discussed in Chapter 3.1.1. Some of the discrepancy is due to not taking the contribution due to drag into account in the calculations of pitching moment from wind tunnel data. This comparison is presented mainly to validate the experimental results and the agreement is close enough to do just that.

3.3.2 Comparison of Effector Configurations

Along with the pitching moment results for the clean airfoil, C_m was calculated for each of the effector configurations; the free-moving effector and each of the six fixed-deployment-angle effectors. The $C_m - \alpha$ curves for the free-moving effector and the fixed-deployment-angle effectors at $\theta = 30°$, $45°$ and $90°$ are compared to the clean airfoil in Figure 3.16.

At pre-stall angles the free-moving effector shows a more negative pitching moment than the clean airfoil while the fixed-deployment-angle effectors all have more positive pitching moments. Recalling the C_p distribution in Figure 3.5 it can be seen that the free-moving effector causes a change in the distribution even as it does not significantly change lift or drag. This change in the distribution is what causes the more negative pitching moment. At these same low alpha angles, the fixed-deployment effectors destroy lift and in doing so cause the opposite effect on C_m.

The region we are most interested in is the high-alpha region, past the stall point for the clean airfoil. This is where the gains are seen in lift and drag, as shown in previous sections. As with the pre-stall

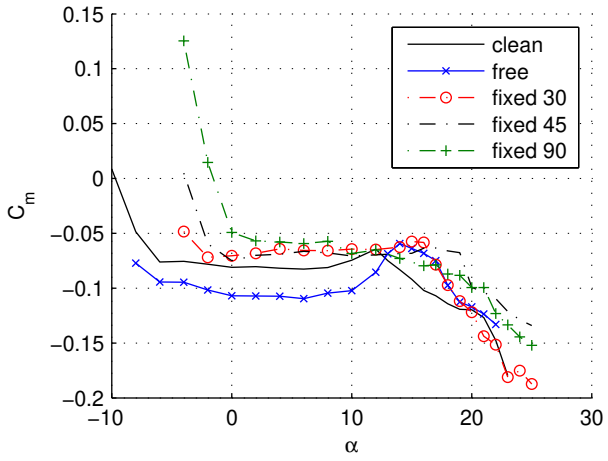

Figure 3.16: $C_m - \alpha$ curves for the clean airfoil and the airfoil with the free-moving effector and the fixed-deployment effectors attached.

region, the C_m trends are the same for the free-moving effector, the fixed-deployment effectors and the clean airfoil. However, C_m for the effector-equipped airfoils, both free-moving and fixed-deployment, is more positive than C_m for the clean airfoil. This is easily explained by the method by which the effector increases lift. C_p forward of the effector is decreased. This moves the center of lift forward on the airfoil at the same time as it increases the lift force. In turn, the pitching moment about the quarter chord becomes more positive. As seen with the $C_d - \alpha$ curves, the curve for the free-moving effector lies between the curves for the fixed-deployment effectors at 30° and 45°. This is another indication that the free-moving effector has an average deployment angle in between 30° and 45°.

While the changes in C_m shown in Figure 3.16 are not significant enough to make the airfoil ineffective, they would have an impact if the effectors were installed on an aircraft. This would need to be taken into account since changes in the pitching moment of an aircraft affect the handling qualities. For instance, at the forward limit for the aircraft center of gravity the elevator angle needed to land, i.e. nearly stall, should not exceed the maximum up elevator angle. However, a change in the pitching moment of the aircraft, due to the change in C_m of the airfoil, would change the needed elevator angle. At the stall point for this airfoil, 12°, the free-moving effector has a more negative C_m than the clean airfoil. This would decrease the aircraft pitching moment and thereby increase the needed elevator angle for landing. On the other hand, the effector causes an increase in C_m above stall, which would decrease the amount of elevator needed to reach those high angles. The specific amount of change in required elevator would depend on the aircraft in question and anyone installing these effectors would need to be careful that the

required elevator still not exceed the maximum available with the effectors attached and at the higher angles of attack made possible by the effectors.

Chapter 4

Flow Visualization

Surface flow visualization allows us to directly see the separation point for many different configurations of the airfoil with and without the effectors. For the clean airfoil, separation can be predicted by XFOIL, but this task is much more difficult for the effector-equipped airfoil. Therefore it is necessary to chart the separation points experimentally. Lift and drag are greatly influenced by separation, so the visualization helps us to better understand the trends seen in lift and drag. Oil flow visualization was done for the clean airfoil and for the airfoil equipped with fixed-deployment effectors. Owing to complications evolving from the movement of the free-moving effector, visualization on that configuration was not attempted. For each of the seven configurations tested, clean and six fixed-deployment angles, oil flow was done at $\alpha = -5°$, $0°$, $5°$, $10°$, $15°$, $20°$ and $25°$. Unfortunately, oil flow visualization has a non-trivial effect on the aerodynamic loads on the model. Barlow et al. [8] show a significant decrease in the lift at all angles of attack when performing oil flow tests. This means that while oil flow will still give us a general idea of the air flow across the surface of the airfoil, it cannot be assumed to correspond exactly to the lift and drag found at the same values of alpha.

With oil flow, the surface flow can be determined by the patterns seen in the oil after a run is completed. On a vertical model, such as the one used in this study (Figure 2.1a), the tendency of the oil, without any airflow, is to flow straight down the model. However, due to the viscosity of the oil, in some cases the oil will simply remain undisturbed if there is no significant airflow. This tendency is what allows us to see separation. After the tunnel has been run, any areas where the oil is flowing straight down or has been left undisturbed are areas of separated flow. Areas where the airfoil has been scrubbed clean are areas of strong attached flow and areas where the oil can be seen to have been pushed in the

downwind direction are areas of slightly less strong, but still attached, flow. Finally, in some cases, the reverse flow due to separation is strong enough to push the oil in the upstream direction.

4.1 The Clean Airfoil

In order to get a good base against which to compare the fixed-deployment effectors, flow visualization was first done on the clean airfoil. At a Reynolds number of 4×10^5 the airfoil used in this study has a laminar separation bubble. The presence of this bubble is confirmed both in XFOIL and by the oil flow. Figure 4.1 shows the results of oil flow on the clean airfoil at $\alpha = 0°$ and $\alpha = 10°$. The separation bubble can be seen in both photos as the area where oil is unaffected by the surface air flow and no downwind flow can be seen. At $\alpha = 0°$ the flow separates at approximately $x/c = 0.48$ and reattaches at approximately $x/c = 0.6$. XFOIL predicts this same separation bubble, but at $\alpha = 2°$. The bubble is greatly decreased at $\alpha = 10°$; extending only from approximately $x/c = 0.1$ to $x/c = 0.15$. At higher angles of attack (15°, 20° and 25°) there is no separation bubble at all.

Laminar separation bubbles are typical of low Reynolds number airflow and are generally the mechanism for transition from a laminar to turbulent boundary layer [11]. Despite almost certainly having a negative effect on the airfoil's drag, the separation bubble's effects on lift are unclear. A large separation bubble, which is tall compared to the boundary layer thickness, will cause a decrease in lift. However, a smaller bubble, which is small compared to the boundary layer thickness, will have very little effect on lift. Given the length of the bubble at $\alpha = 0°$ it seems likely that it is indeed causing a decrease in lift, but the much smaller bubble at $\alpha = 10°$ may have little or no effect.

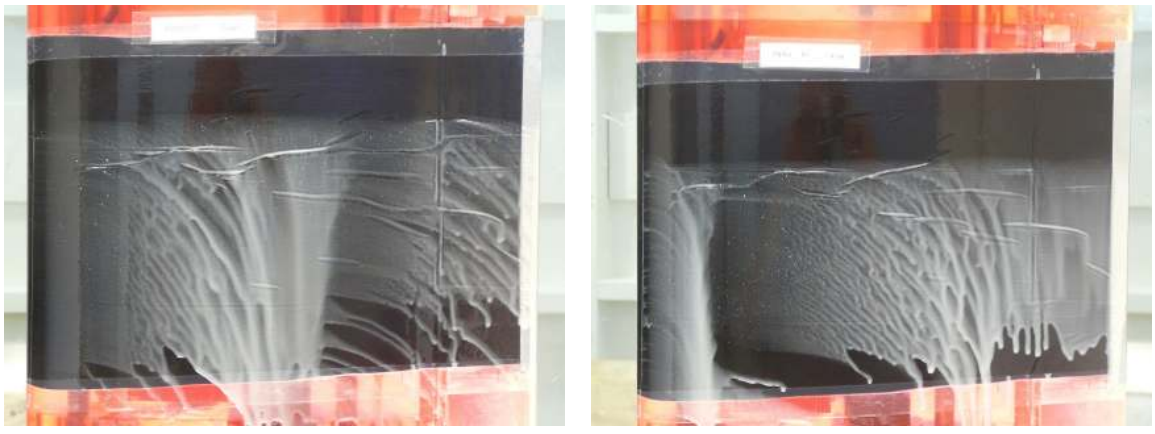

(a) (b)

Figure 4.1: Oil flow on the clean airfoil at (a) $\alpha = 0^o$ and (b) $\alpha = 10^o$.

Although the separation bubble is an interesting feature to note, and may have some effect on the effector which will be discussed later, the more important feature observed from oil flow visualization is the final separation point, where the flow separates from the airfoil and does not reattach. No significant suction is usually produced by the airfoil after the separation point so the location of this point directly affects the airfoil's lift coefficient. From the oil flow tests it was seen that flow remains attached to the airfoil, all the way to the trailing edge, through $\alpha = 5°$. At $\alpha = 10°$ the flow separates at $x/c = 0.75$. At $\alpha = 15°$ separation occurs at $x/c = 0.34$. XFOIL shows separation at $x/c = 0.75$ to occur at $\alpha = 12°$. At $\alpha = 20°$ and $25°$ there is no attached flow on the airfoil. This is not unsurprising given that this airfoil stalls at $\alpha = 12°$. The notable trend with separation point is that once the flow starts to separate, between $\alpha = 5°$ and $\alpha = 10°$, the separation point continues to migrate forward on the airfoil as alpha is increased. This is typical for separation on most airfoils.

4.2 Fixed-Deployment-Angle Effectors

The main goal of the effector is to increase the lift produced by the airfoil, especially in the high alpha range, beyond normal stall. As was mentioned in Section 4.1, separation point is a good indication of how much lift is being produced. Later separation means lift is being produced along more of the airfoil. In Section 3.1.3 it was shown that the fixed-deployment-angle effectors act like spoilers in the low alpha range, but increase lift above the clean airfoil once they become active. Therefore it is expected that the separation point for the fixed effectors will be earlier than the clean airfoil at angles of attack below their activation point (Section 3.1.3) and later after that point. Figure 4.2 shows the separation points seen in oil flow visualization. As expected, all of the fixed-deployment-angle effectors have significantly earlier separation points for α from $-5°$ to $10°$. In fact the separation points at $\alpha = -5°$ move forward on the airfoil as deployment angle is increased. Again this goes along with the results from lift: higher deployment angles produce less lift at low alpha.

At $\alpha = 15°$ in the flow visualization, the separation point is later than the clean airfoil for all the fixed effectors with the exception of $\theta = 90°$. This suggests that all of the fixed effectors are producing lift along more of the airfoil surface than the clean airfoil and should therefore be producing more lift than the clean airfoil. This might be true, but it does not agree with the lift curves in Figure 3.7. However, there are several influences on the lift to consider. First is the change in lift due to the oil flow setup. In Figure 3.7 it can be seen that only the fixed effectors at $\theta = 15°$ and $\theta = 30°$ produce more lift than the

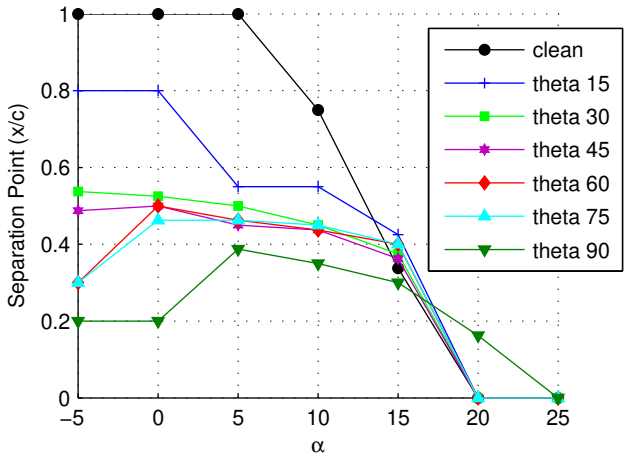

Figure 4.2: Separation points from oil flow visualization for the clean airfoil and the airfoil with each of the fixed-deployment-angle effectors.

clean airfoil at $\alpha = 15°$, but we cannot assume that what we see in oil flow corresponds exactly to the lift results. So the late separation may indeed indicate more lift being produced. Another influence of note is the laminar separation bubble. For the clean airfoil at $\alpha = 15°$ there is no separation bubble. This is also true for the fixed effectors at $\theta = 15°$ and $\theta = 30°$. But for the four highest deployment angles a separation bubble of 5 to 9 percent of the chord is present (Figure 4.3). This bubble could be causing a detrimental effect on lift and therefore keeping the lift produced by the fixed effectors less than that for the clean airfoil even though the separation point is farther aft.

Another deviation from the lift results is that all but the $\theta = 90°$ effector are completely stalled at $\alpha = 20°$. There is no oil flow across the airfoil's upper surface, indicating that separation occurs at the leading edge. However, Figure 3.7 shows that lift is still being produced by several of the configurations. Also drag tests showed that the dramatic increase in drag usually associated with stall does not occur until after $\alpha = 20°$ for the fixed effector at $\theta = 60°$ or $\theta = 75°$ (Figure 3.13). This discrepancy is assumed to be caused by the oil flow itself.

Despite the differences between results from lift and drag and those from the visualization, the trends seen in the visualization are as expected and help to explain how the effector causes an increase in lift at post stall angles of attack. The separation point is later for the effector-equipped airfoil, at high α, than it is for the clean airfoil. So along with allowing lower pressure in front of the effector, separation is delayed, adding to the lift enhancement produced by the effector.

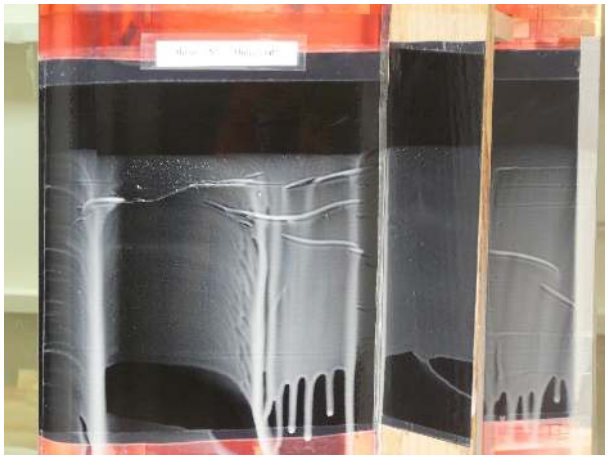

Figure 4.3: Oil flow on the fixed-deployment-angle effector at $\theta = 60^o$ and $\alpha = 15^o$. The laminar separation bubble can be seen from $^x/_c = 0.0875$ to 0.1375.

The oil flow visualization also showed some interesting properties of the flow across the effector. In Figure 4.3 the airflow is separated in front of the effector, but reattaches on the effector surface. It can be seen in the picture that from the base to approximately a quarter of the way up the effector the flow is reversed, flowing down the effector back towards the airfoil surface. After this point the oil is pushed up the effector towards the trailing edge, indicating attached flow in the downstream direction. For lower deployment angles the flow is attached and flowing in the downstream direction all across the effector (Figure 4.4), whereas at the higher deployment angles there is separation before the effector and reattachment somewhere between a quarter and halfway up the effector. This allows an interesting look into the airflow just off the airfoil surface. It appears that there is a pocket of separation in front of the effector with reversed flow. The point of reattachment on the effector seems to indicate the size and height of this separated pocket.

Figure 4.4: Oil flow on the fixed-deployment-angle effector at $\theta = 30^o$ and $\alpha = 10^o$. Flow is attached on the effector as seen by the downstream movement of the oil.

Chapter 5

CFD - Immersed Boundary Approach

The basic idea of the immersed boundary method is to resolve the flow features around a given geometry that has been embedded into a computational mesh without requiring that the boundary points coincide with the mesh nodes. These methods can be extremely useful for complex geometries such as the airfoil and effector. The idea is to resolve flow around these complex bodies while avoiding the difficulties associated with grid adaptation, overset grids, or moving grids. With the immersed boundary method a designer only needs a Cartesian mesh along with the cloud of points that define the surface geometry. The method implemented here follows that of Mohd-Yusof [12, 13], in which the methods developed by Peskin [14] are interpreted as a direct momentum forcing. The effects of the immersed boundary are included by defining band cells, those surrounding the body, and prescribing conditions at these points. The conditions prescribed mimic the movement of the surface, shearing effect, and heat transfer. The code, a variation of one developed by Choi et al. [15], solves the incompressible Navier-Stokes equations utilizing the finite volume method; a greater detail of the coding algorithm is in the 2007 paper by Choi et al [15]. The code used for this study also includes the Spalart-Allmaras turbulence model [16].

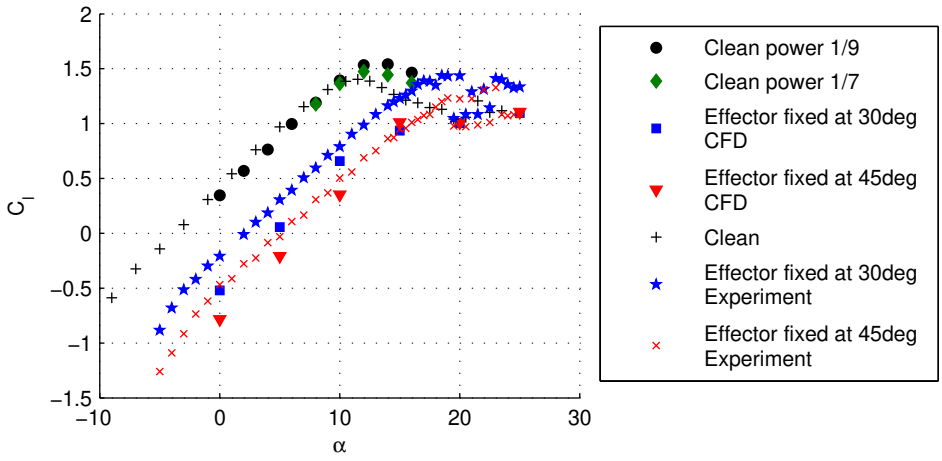

Figure 5.1: CFD generated lift curves as compared to experimental lift curves. The "power 1/7" and "power 1/9" refer to a parameter which influences how well the flow stays attached. The effector fixed CFD runs were both done with power 1/7.

5.1 Validation

As of now the code is unable to handle the free-moving effector so it was used to simulate the flow around the clean airfoil and the airfoil with the effector attached at fixed-deployment angles. Due to time constraints the simulation was only done for the effector fixed at 30° and 45°. Results include $C_l - \alpha$ curves as well as contour plots showing the airflow's downstream velocity. These contour plots were created for the same angles as were used in the oil flow visualization, but only for the airfoil with the fixed-deployment effectors, not for the clean airfoil. These angles were chosen in order to best compare the surface flow, shown in oil flow, to the surrounding flow, shown by CFD. The lift curve slopes generated by CFD provide us with a measure of how closely the simulation matches wind tunnel tests (Figure 5.1). The lift for the clean airfoil matches quite well up to stall. However, the simulation stalls at a slightly higher lift coefficient than the experiment and does not drop quite as quickly. The CFD lift curves for both fixed effectors predict lower C_l in the low-alpha range than the experimental curves and interestingly they start to converge at $\alpha = 15°$ and do not show the significant advantages in lift produced in the wind tunnel. However, at low-α, they do show the same trend of decreasing C_l as deployment angle increases, and by approximately the same amount.

At this time the differences in the CFD results and the experimental results are not understood. Due to these differences, the contour plots generated by CFD simulation must regarded much the same way

as the oil flow visualization. They can help to elucidate how the effector works and show general trends for the effectors, but they cannot be considered to compare exactly with the lift and drag results from wind tunnel experiments.

5.2 CFD contours

Contour plots generated by CFD show the flow field around the airfoil. This gives us a good comparison with the oil flow visualization which shows the surface flow across the airfoil. From the flow field we can see separation by noting where there is reversed flow, separation will occur just at the front of any reversed flow section. Examination of the contour plots (not shown) reveals that for $\alpha = 0°$ through $\alpha = 10°$ the separation points match well to those shown in Figure 4.2 for both the 30° and 45° deployment angles. At the two higher alphas, 20° and 25°, both CFD and oil flow show separation at the leading edge of the airfoil. However at $\alpha = 15°$ for some reason the separation point shown in CFD is much earlier on the airfoil than that seen in oil flow.

Another feature seen in oil flow visualization was the laminar separation bubble, clearly shown for this airfoil at the test Reynolds number of 4×10^5. This separation bubble also shows up for the airfoil with fixed-deployment-angle effectors. However, the power law for the CFD simulation assumes a turbulent boundary layer throughout and is therefore unable to model laminar separation bubbles. As a result, the contours generated by CFD do not show any separation bubbles. This may be part of the reason for the differences between the CFD results and those from the wind tunnel.

The last feature of the CFD contour plots is the position of the effector within the separated region. Meyer et al. [6] claim that the optimal position of the effector is at a deployment angle which lets the top of the effector just touch the edge of the boundary layer. From the CFD plots in Figure 5.2 we can see that when the effector is deployed there is a separated region in front of it. So the optimal deployment angle will be the angle for which this forward separated region is large enough to just reach the top of the effector. This is the case for the effector deployed to 45° at $\alpha = 15°$. However, it is also obvious from the contour plots that the forward separation grows as alpha is increased; this is intuitive as the separation for the clean airfoil also grows and moves forward as alpha increases. Thus, the changing separation region needs to be met with an effector deployed at changing angles in order to keep the optimal situation with the top of the effector touching the edge of the boundary layer. This relates back to the free-moving effector which was seen to gradually deploy as alpha increased and to the earlier

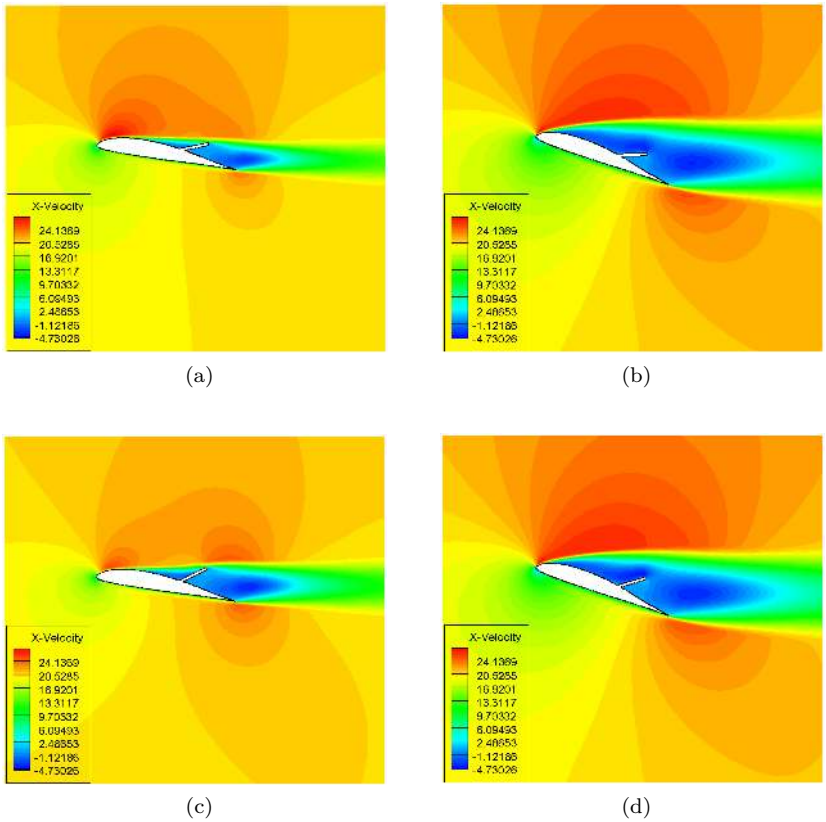

Figure 5.2: CFD contour plots of the effector at $\theta = 30^o$ (a and b) and $\theta = 45^o$ (c and d) for $\alpha = 10^o$ (a and c) and $\alpha = 20^o$ (b and d). The contours show flow velocity in the downstream (x) direction.Velocity units are m/s.

tests of the fixed-deployment effectors where the benefits to lift and drag occurred at successively higher alphas for successively higher deployment angles.

Although the simulations were not extensive enough to find the optimal deployment angle for each alpha, they do show us that for the $\theta = 45°$ effector that angle is 15° (Figure 5.3) and the effector is over-deployed at lower alphas and under-deployed at higher alphas. For $\theta = 30°$ the effector is over-deployed for $\alpha = 10°$ and below and under-deployed for $\alpha = 15°$ and above. This can be seen in the contours (Figure 5.2) by noting the blue reversed flow regions. When the reversed flow region in front of the effector is the same height as the effector, the deployment angle is optimal. When the forward separation region extends over the top of the effector, connecting to the rear separation region, the effector is under-deployed. When that forward separation region does not reach the top of the effector, the effector is over-deployed. Figure 5.2 shows the contour plots for $\alpha = 10°$ and $\alpha = 20°$ for both the 30° and 45° fixed-deployment effectors.

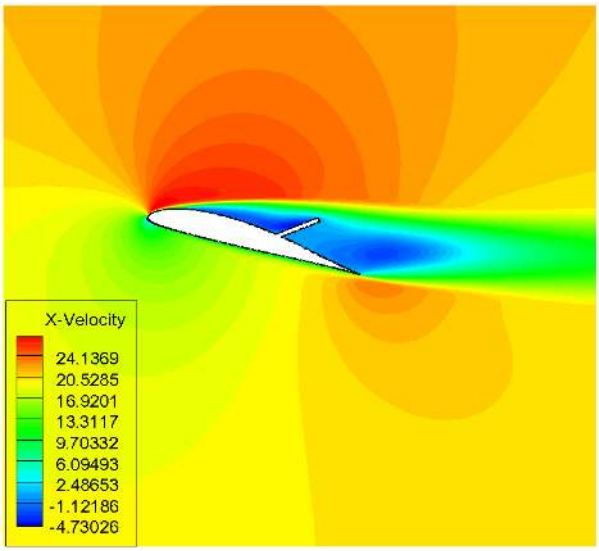

Figure 5.3: CFD contour plot for the fixed-deployment effector at $\theta = 45^o$ and $\alpha = 15^o$. The contours show flow velocity in the downstream (x) direction. Velocity units are $^{m}/_{s}$.

Chapter 6

Conclusions

The results of attaching a lift enhancing effector to the upper surface of a 2-D airfoil have been presented in this thesis. The investigation used both free-moving and fixed-deployment-angle effectors. The fixed-deployment effectors were useful to study the influence on the flow field and airfoil surface pressures while having control over the deployment angle. Both lift and drag are dramatically improved for angles of attack past the airfoil's normal stall angle. However, the improvements in lift do not seem to continue past a deployment angle of 60° and the free-moving effector has a drag curve between the curves for the 30° and 45° fixed effector. Since allowing the effector to rotate past 90° proved detrimental, and the above arguments suggest that allowing it to rotate past 60° does not provide any additional benefit, it is inferred that limiting the effector to a maximum deployment of 60° would be the optimal configuration.

At high angles of attack the effector lifts off the airfoil surface and begins influencing the flow. C_p distributions show that the effector causes a step-like pressure change and thereby allows lower pressures forwards of the effector as well as a slightly higher trailing edge pressure. This is what has been called the pressure-dam effect and is the mechanism by which the effectors delay separation and increase lift. It was shown that the pitching moment increases as a result of the effector's influence, but it does not change enough to increase or decrease the utility of the effector.

Further work is needed to improve the agreement between CFD predictions and wind tunnel tests, but the combination of CFD and oil flow visualization in this study does serve to confirm the separation delay caused by the effector at high angles of attack, past the clean airfoil's stall condition. It also helps to illustrate the flow-field conditions necessary for optimal deployment, which appears to coincide with

the condition at which the top of the effector just touches the edge of the separated boundary layer. The results from the fixed-deployment-angle effectors show that changes in angle of attack will cause a change in the optimal deployment angle of the effector. Remarkably, the free-moving effector seems to automatically deploy to the optimal angle, up to the point where the separated region becomes too large and the effector flips over. So a free-moving effector, equipped with some device to limit maximum deployment to 60°, will create a much gentler stall for the airfoil, allowing it to go to much higher angles of attack without loss of lift.

Bibliography

[1] Bechert, D. W., Bruse, M., Hage, W., and Meyer, R., "Fluid mechanics of biological surfaces and their technological application." *Die Naturwissenschaften*, Vol. 87, No. 4, April 2000, pp. 157–71.

[2] Bechert, D., Bruse, M., Hage, W., and Meyer, R., "Biological surfaces and their application–laboratory and flight experiments on drag reduction and separation control," AIAA paper 1997-1960, 1997.

[3] Carruthers, A. C., Thomas, A. L. R., and Taylor, G. K., "Automatic aeroelastic devices in the wings of a steppe eagle Aquila nipalensis." *The Journal of Experimental Biology*, Vol. 210, No. 23, December 2007, pp. 4136–49.

[4] Kernstine, K., Moore, C., Cutler, A., and Mittal, R., "Initial Characterization of Self-Activated Movable Flaps,'Pop-Up Feathers'," AIAA paper 2008-369, 2008.

[5] Schlüter, J. U., "Lift Enhancement at Low Reynolds Numbers Using Self-Activated Movable Flaps," *Journal of Aircraft*, Vol. 47, No. 1, January 2010, pp. 348–351.

[6] Meyer, R., Hage, W., Bechert, D. W., Schatz, M., Knacke, T., and Thiele, F., "Separation Control by Self-Activated Movable Flaps," *AIAA Journal*, Vol. 45, No. 1, Jan. 2007, pp. 191–199.

[7] Traub, L. W. and Jaybush, L., "Experimental Investigation of Separation Control Using Upper-Surface Spoilers," *Journal of Aircraft*, Vol. 47, No. 2, March 2010, pp. 714–718.

[8] Barlow, J., Rae, W., and Pope, A., *Low-speed wind tunnel testing*, John Wiley & Sons, 1999.

[9] Jepson, J. K. and Gopalarathnam, A., "Experimental Demonstration of a Sense-and-Adapt Approach for Automated Adaption of a Wing with Multiple Trailing-Edge Flaps," AIAA paper 2007-4062, 2007.

[10] Bramesfeld, G. and Maughmer, M., "Experimental investigation of self-actuating, upper-surface, high-lift-enhancing effectors," *Journal of Aircraft*, Vol. 39, No. 1, 2002, pp. 120–124.

[11] Liebeck, R. H., "Subsonsic Airfoil Design," *Applied Computational Aerodynamics*, edited by A. R. Seebass, Vol. 125, AIAA, 1990, pp. 133–165.

[12] Mohd-Yusof, J., "Development of Immersed Boundary Methods for Complex Geometries," *Center for Turbulence Research Annual Research Briefs*, 1998, pp. 325–336.

[13] Mohd-Yusof, J., "Combined Immersed Boundaries/B-splines Methods for Simulation of Flows in Compex Geometries," *Center for Turbulence Research Annual Research Briefs*, 1997, pp. 317–327.

[14] Peskin, C. S., "Flow Patterns Around Heart Valves: A Numerical Method," *Journal of Computational Physics*, Vol. 10, No. 2, October 1972, pp. 220–252.

[15] Choi, J.-I., Oberoi, R. C., Edwards, J. R., and Rosati, J. A., "An Immersed Boundary Method for Complex Incompressible Flows," *Journal of Computational Physics*, Vol. 224, No. 2, June 2007, pp. 757–784.

[16] Spalart, P. and Allmaras, S., "A one-equation turbulence model for aerodynamic flows," *La recherche aérospatiale*, Vol. 1, No. 1, 1994, pp. 5–21.